

Nowcasting of Wind in the Venice Lagoon Using WRF-FDDA

Dario Conte ^{1,*}, Alessandro Tiesi ¹ , Will Cheng ², Alvisè Papa ³  and Mario Marcello Miglietta ¹ ¹ National Research Council-Institute of Atmospheric Sciences and Climate (CNR-ISAC), 35127 Padua, Italy² National Center for Atmospheric Research, Boulder, CO 80307, USA³ Centro Previsioni e Segnalazioni Maree, 30100 Venice, Italy

* Correspondence: d.conte@isac.cnr.it

Abstract: The Four-Dimensional Data Assimilation module (FDDA) is used in combination with the WRF model for the analysis of two case studies of high tide (on 4 April 2019 and on 12 November 2019) that affected the Venice Lagoon in the recent past. The system is implemented in the perspective of an operational use for nowcasting of 10 m wind, which will be part of a numerical system aimed at the forecast of the sea level height in the Venice Lagoon. The procedure involves the assimilation of data from meteorological surface stations distributed within the Venice Lagoon and in the open northern Adriatic Sea in front of the lagoon, as well as the radiosonde profiles available within the simulation domain. The two cases were selected considering that the real-time forecasts missed their evolution, and the sea level height was significantly underpredicted. The comparison of the simulated wind with the observations shows a fairly good agreement over short time scales (1–2 h) in both cases; hence, the WRF-FDDA system represents a promising tool and a possibly valuable support to the decision makers in case of high tide in the Venice Lagoon.

Keywords: data assimilation; numerical modeling; severe weather forecast; Venice lagoon



Citation: Conte, D.; Tiesi, A.; Cheng, W.; Papa, A.; Miglietta, M.M. Nowcasting of Wind in the Venice Lagoon Using WRF-FDDA. *Atmosphere* **2023**, *14*, 502. <https://doi.org/10.3390/atmos14030502>

Academic Editor: Massimiliano Burlando

Received: 1 February 2023

Revised: 28 February 2023

Accepted: 2 March 2023

Published: 4 March 2023



Copyright: © 2023 by the authors. Licensee MDPI, Basel, Switzerland. This article is an open access article distributed under the terms and conditions of the Creative Commons Attribution (CC BY) license (<https://creativecommons.org/licenses/by/4.0/>).

1. Introduction

Coastal vulnerability represents an issue in the protection of population living in coastal urban areas and of port infrastructures from natural hazards acting on different temporal and spatial scales. Astronomical tides, seiches, storm surges, and meteotsunamis are potential risk factors characterized by a large range of time variability, from minutes/hours (mesoscale) to weeks/months (planetary scale), and their combination can cause relevant effects on the sea level [1,2].

The Mediterranean Sea is a basin extremely vulnerable to such events, due to the presence of several anthropic activities along its coasts. At the center of the Mediterranean Sea, on its northern side, the Adriatic Sea is a semi-enclosed basin surrounded by the Apennines Mountain range to the west and the Dinaric Alps to the east, closed at the northern end by the Po Valley and the eastern Alps. Such a geographical conformation is prone to channel southerlies from the Otranto Strait to the northern coast, which may possibly cause wind waves and increase sea level height [3,4].

Therefore, the Venice Lagoon, situated on the northern Adriatic coast, is extremely exposed to coastal hazards that may affect the resident population, the infrastructures, and their unique historical heritage [5]. The monitoring and the surveillance service of the Venice lagoon is managed by the Tide Forecast and Early Warning Center of the city of Venice (Centro Previsione e Segnalazione Maree; CPSM) and the Italian Institute for Environmental Protection and Research (ISPRA), through two tide gauge and meteorological surface station networks within and in the surroundings of the Venice Lagoon.

Table 1 lists the most significant high-tide events that have occurred since 1936, accounting for episodes in which the sea level in the lagoon was higher than 140 cm. High tides generally occur during the fall and early winter, with a higher concentration in the months of November and December. Moreover, the majority of the episodes have occurred

in the last two decades. In fact, global warming is expected to increase the occurrence of these events due to the rising of the average sea level and the intensification of severe meteorological conditions favorable to meteotsunamis [6–8].

Table 1. The most significant high-tide events (above 140 cm) that have occurred since 1936 (available at <https://www.comune.venezia.it/it/content/le-acque-alte-eccezionali>, accessed on 15 November 2022).

Date	Height (cm)	Date	Height (cm)
16 April 1936	147	16 November 2002	147
12 November 1951	151	1 December 2008	156
15 October 1960	145	23 December 2009	144
4 November 1966	194	25 December 2009	145
3 November 1968	144	24 December 2010	144
17 February 1979	140	1 November 2012	143
22 December 1979	166	11 November 2012	149
1 February 1986	158	12 February 2013	143
8 December 1992	142	29 October 2018	156
6 November 2000	144	12 November 2019	187 ¹

¹ Measured at Punta Salute on the Grand Canal side.

To prevent the occurrence of high tides within the Venice Lagoon, the Italian government funded the construction of mobile barriers at its inlet (MOSE—Experimental Electromechanical Module—project). The activation of the barriers is decided according to the tide forecast provided by CPSM. Such forecasts strongly depend on the meteorological predictions, particularly on the wind. The usefulness of the system was demonstrated on the morning of 22 November 2022, at the Lido port mouth, when the tide reached 204 cm, the highest value in the historical record, but the correct activation of the barriers prevented Venice from being flooded.

In the present work, two case studies (on 4 April 2019 and on 12 November 2019) of high tide are analyzed using the Weather Research and Forecasting (WRF) model. The two cases were selected considering that the real-time forecasts missed their severity, such that the sea level height was significantly underestimated [9]. The first event was characterized by an unpredicted increase in the tide height, because of the passage of a small cold front that the models misrepresented. Although the event did not cause an extreme tide, the wrong real-time prediction and its occurrence in spring represent make this case study unusual and worth of deeper investigation. The second event was responsible for the second highest tide in historical record; after the Bora wind pushed the water to the southern part of the lagoon, a small-scale cyclone, which the numerical models were not able to properly simulate, rapidly crossed the lagoon generating intense southerlies.

The Four-Dimensional Data Assimilation (FDDA) module, which is designed for the ingestion of different observations (from surface stations, radiosondes, profilers, etc.), is used to nudge the simulations toward the observations. In the case studies presented here, FDDA employs surface data from the meteorological station network in the Venice Lagoon and two meteorological stations offshore, located just in front of the lagoon. Additionally, the vertical profiles of radiosondes in the outer simulation domain are ingested. The surface data are assimilated in the nudging process and also used for model verification after the nudging is switched off.

The present work is organized as follows: Section 2 describes the setup of the WRF model, the FDDA module, and the experimental data. Section 3 describes the two case studies analyzed here, which occurred on 4 April 2019 and 12 November 2019. Section 4 contains the discussion and conclusions.

2. Tools, Experimental Setup, and Data

The present section focuses on the description of the modeling tools implemented for the meteorological simulations.

2.1. WRF Model

The meteorological model WRF-ARW, version 4.0 [10], is used to perform the hindcasts of the two case studies described in Section 3.

The domain setup of the model consists of the two one-way nested domains shown in Figure 1 (left hand side), with grid spacings of 9 km (Grid 1; G1) and 3 km (Grid 2; G2), 250×220 and 385×235 horizontal grid points, respectively, and 41 vertical hybrid levels (terrain following near the ground and pressure surfaces above) for both grids.

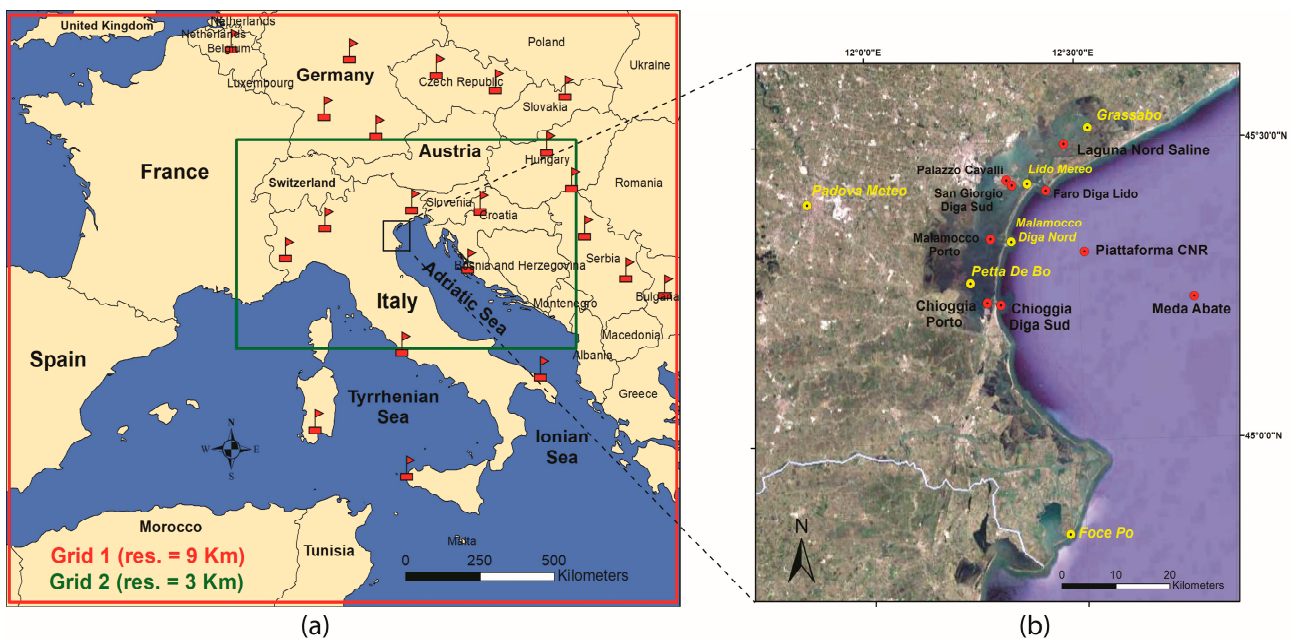


Figure 1. (a) Domains used in the WRF model simulations with grid spacing of 9 km (red rectangle) and 3 km (green rectangle). The red flags represent the position of the radiosondes for which the bulletins at 12:00 UTC, 12 November 2019, are available. (b) Zoomed-in view of the Venice Lagoon and its surroundings, with identification of the weather surface stations managed by CPSM (red marks) and those managed by the ISPRA Institute (yellow marks). The map background is a satellite image acquired by Google Earth on 14 December 2015.

The parameterization schemes include the Thompson microphysics scheme [11], the RRTM longwave radiation [12], the Dudhia shortwave radiation [13], the revised MM5 surface layer scheme [14,15], the unified Noah land-surface model [16], and the YSU boundary layer [17]. The Kain–Fritsch cumulus scheme [18] is active only in Grid 1, although preliminary experiments have shown that the activation of cumulus parameterization also in Grid 2 produces only minor changes in the case of November 2019 [9].

Initial and boundary conditions are provided by the Global Forecast System (GFS) analysis/forecasts (<https://www.ncei.noaa.gov/products/weather-climate-models/global-forecast>) (accessed 1 February 2020), at a grid resolution of 0.25° , and with 34 pressure levels. Lateral boundary conditions are updated every 3 h.

2.2. FDDA

The Four-Dimensional Data Assimilation (FDDA) is a nudging scheme designed for the WRF model [19]. It modifies the prognostic equations for wind, humidity, and temperature, by adding a weighted nudging term that leads the model toward the observed state. The detailed description of the FDDA technique is provided in Appendix A.

Recently, Chen et al. (2021) [20] used the WRF-FDDA numerical system for the assimilation of Doppler radar wind in the case of the Typhoon Nesat that hit Taiwan in July 2017, while Sun et al. (2022) [21] applied the WRF-FDDA to assimilate the data retrieved from the Lightning Mapping Imager (LMI) onboard the geostationary satellite Fengyun-4A for the simulation of two mesoscale convective systems that affected Hainan Island in Southern China in August 2019. In both cases, the results showed a positive impact of the assimilation on the simulation results.

2.3. Data

The observations employed for the assimilation in the present study are presented in Figure 1. The 14 meteorological surface stations within and around the Venice lagoon are shown in the right panel; of these, nine surface stations, identified by the red circles, are managed by CPSM, while the remaining five stations (yellow circles) are managed by ISPRA. They provide sea level pressure, 2 m temperature and humidity, and 10 m wind with a time frequency of 5 min in near real time; unfortunately, some of them were out of service during the case studies considered here.

Moreover, the observations of the radiosondes available within the outer domain are assimilated, as they represent accurately the vertical profiles of temperature, humidity, and wind.

Sounding data are generally available at 00:00 UTC and 12:00 UTC; those used in this study are downloaded from the University of Wyoming—Department of Atmospheric Science (<http://weather.uwyo.edu/upperair/sounding.html>, accessed on 15 May 2022). As an example, red flags in Figure 1 (left panel) show the geographic position of the sounding stations for which bulletins are available at 12:00 UTC, 12 November 2019, and which were ingested in the assimilation process for that case study.

3. Case Studies

3.1. Introduction

Two case studies of high tide that occurred in the Venice Lagoon on 4 April and 12 November 2019 are analyzed here. Considering the small scale of the meteorological features in these cases, even a small error in time or space caused large errors in the prediction of wind and pressure fields, which, combined with the complex morphology of the lagoon, produced errors of several cm in the simulation of sea level height.

For each case study, a set of numerical simulations is performed, as listed in Table 2. Among them, the control run named “WRFT0” consists of a WRF model simulation in which the WRF-FDDA module is turned off.

For WRF model simulations WRFT $hh \dots$, the observation nudging is active from the beginning of the run until the time $hh:00$ (where hh and 00 are the hour and minute, respectively, in UTC), which is either a few hours before or during the phase the high tide reaches its maximum.

Table 2. List of simulations.

Simulations List										
Case Study	Simulation Name	Time Start (UTC)	Length (hours)	FDDA Grid 9 km	FDDA Grid 3 km	Time FDDA Turned off (UTC)	Reduced Acquisition Time Window	Horizontal Radius of Influence (km)	Type of Nesting	obs_coef_wind
4 April 2019	WRFT0	00:00	24	OFF	OFF	00:00	NO	75, 20	One Way	$7 \times 10^{-3}, 8 \times 10^{-3}$
	WRFT20_rinxy1	00:00	24	ON	ON	20:00	NO	35, 10	One Way	$7 \times 10^{-3}, 8 \times 10^{-3}$
	WRFT20_rinxy2	00:00	24	ON	ON	20:00	NO	25, 6	One Way	$7 \times 10^{-3}, 8 \times 10^{-3}$
	WRFT20_G1OFF_G2ON_TW	00:00	24	OFF	ON	20:00	NO	75, 20	Two Way	$7 \times 10^{-3}, 8 \times 10^{-3}$
	WRFT20_G1OFF_G2ON_TW_R	00:00	24	OFF	ON	20:00	YES	75, 20	Two Way	$7 \times 10^{-3}, 8 \times 10^{-3}$
	WRFT20_G1ON_G2OFF	00:00	24	ON	OFF	20:00	NO	75, 20	One Way	$7 \times 10^{-3}, 8 \times 10^{-3}$
	WRFT20_G1ON_G2OFF_R	00:00	24	ON	OFF	20:00	YES	75, 20	One Way	$7 \times 10^{-3}, 8 \times 10^{-3}$
	WRFT20_G1OFF_G2ON	00:00	24	OFF	ON	20:00	NO	75, 20	One Way	$7 \times 10^{-3}, 8 \times 10^{-3}$
	WRFT20_G1OFF_G2ON_R	00:00	24	OFF	ON	20:00	YES	75, 20	One Way	$7 \times 10^{-3}, 8 \times 10^{-3}$
	WRFT20_W	00:00	24	OFF	ON	20:00	NO	75, 20	One Way	$6 \times 10^{-4}, 6 \times 10^{-4}$
	WRFT18	00:00	24	ON	ON	18:00	NO	75, 20	One Way	$7 \times 10^{-3}, 8 \times 10^{-3}$
	WRFT18_R	00:00	24	ON	ON	18:00	YES	75, 20	One Way	$7 \times 10^{-3}, 8 \times 10^{-3}$
	WRFT19	00:00	24	ON	ON	19:00	NO	75, 20	One Way	$7 \times 10^{-3}, 8 \times 10^{-3}$
	WRFT19_R	00:00	24	ON	ON	19:00	YES	75, 20	One Way	$7 \times 10^{-3}, 8 \times 10^{-3}$
	WRFT20	00:00	24	ON	ON	20:00	NO	75, 20	One Way	$7 \times 10^{-3}, 8 \times 10^{-3}$
	WRFT20_R	00:00	24	ON	ON	20:00	YES	75, 20	One Way	$7 \times 10^{-3}, 8 \times 10^{-3}$
	WRFT21	00:00	24	ON	ON	21:00	NO	75, 20	One Way	$7 \times 10^{-3}, 8 \times 10^{-3}$
WRFT21_R	00:00	24	ON	ON	21:00	YES	75, 20	One Way	$7 \times 10^{-3}, 8 \times 10^{-3}$	
12 November 2019	WRFT0	12:00	12	ON	ON	12:00	NO	75, 20	One Way	$7 \times 10^{-3}, 8 \times 10^{-3}$
	WRFT21	12:00	12	ON	ON	21:00	NO	75, 20	One Way	$7 \times 10^{-3}, 8 \times 10^{-3}$
	WRFT21_R	12:00	12	ON	ON	21:00	YES	75, 20	One Way	$7 \times 10^{-3}, 8 \times 10^{-3}$
	WRFT22	12:00	12	ON	ON	22:00	NO	75, 20	One Way	$7 \times 10^{-3}, 8 \times 10^{-3}$
	WRFT22_R	12:00	12	ON	ON	22:00	YES	75, 20	One Way	$7 \times 10^{-3}, 8 \times 10^{-3}$

Due to the limited model skill in the case of 4 April 2019, additional tuning simulations are considered only for this case. A set of simulations (ending with *_R* in Table 2) is performed changing *obs_twindo*, the parameter controlling the extension of the time window during which the weighting function is different from 0 (Appendix A). In this set of experiments, only for surface data acquisition, the parameter value is reduced from 0.667 h (about 40 min) to $\text{obs_sfact} \times \text{obs_twindo} = 0.667 \times 0.083 = 0.055$ h (about 3.3 min) (cfr. simulations of type A with type B in Table A1). In fact, considering the high temporal frequency of the surface data (every 5 min) and the rapid meteorological evolution in the cases we considered, the nudging to observations for a longer time may be detrimental to the simulation skill, and the results may benefit from a shorter time window. Additional sensitivity tests were performed reducing the horizontal radius of influence *obs_rinxy* to one-half (run WRFT20_rinxy1) or one-third (run WRFT20_rinxy2) of the value used in the control run, i.e., 75 km in the outer and 20 km in the inner domain. Furthermore, a test was undertaken (run WRFT20_W) reducing the weights used to nudge the variables to be assimilated.

In the control run, the nudging is performed in both the outer and the inner domains, using a one-way nesting configuration. In a set of sensitivity experiments, the nudging setup was modified by activating the nudging only in the outer domain (WRFT20_G1ON_G2OFF) or only in the inner domain (WRFT20_G1OFF_G2ON); in the latter case, a two-way nesting configuration was also tested (WRFT20_G1OFF_G2ON_TW).

In the next section, the ability of different nudging configurations is investigated with the aim of improving the predictive skill of the model, looking in particular at the second part of the run, when the model is no longer nudged. The study was carried out by comparing the simulated values of zonal and meridional 10 m wind with the corresponding observations at the stations in the Venice Lagoon and its surroundings (Figure 1b).

3.2. Case Study 1: 4 April 2019

3.2.1. Description

On 4 April 2019, around 21:00 UTC, an anomalous time evolution of the sea level height was observed with respect to the normal (astronomical) tidal cycle, which was not represented in the real-time meteorological numerical simulations available at that time. Figure 2 shows the sea level height observed in two tide stations, Piattaforma CNR, which is in the open sea in front of the Venice lagoon, and Punta Salute, which is between the weather stations of Palazzo Cavalli and San Giorgio Diga Sud (Figure 1b), close to Venice historical center.

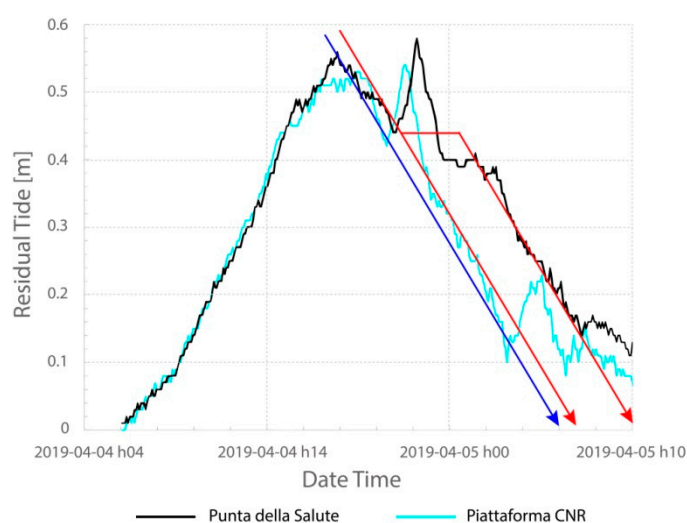


Figure 2. Residual tide over “Piattaforma CNR” and “Punta salute” stations, on 4–5 April 2019. Blue and red arrows represent the linear tidal trend (time is expressed in UTC+1).

In both stations, the lowering of the sea level, due to the astronomical tide, was abruptly interrupted by a brief perturbation, which produced a temporary rise for about 40 min, after which the sea level height restarted to fall.

At Piattaforma CNR station, the wind speed does not show extreme values, as it remains below $15 \text{ m}\cdot\text{s}^{-1}$, but a rapid increase in the zonal wind component is observed around 21:00 UTC (Figure 3, panel a3). Thus, we suppose this meteorological perturbation is responsible for the change in the evolution of the sea level height.

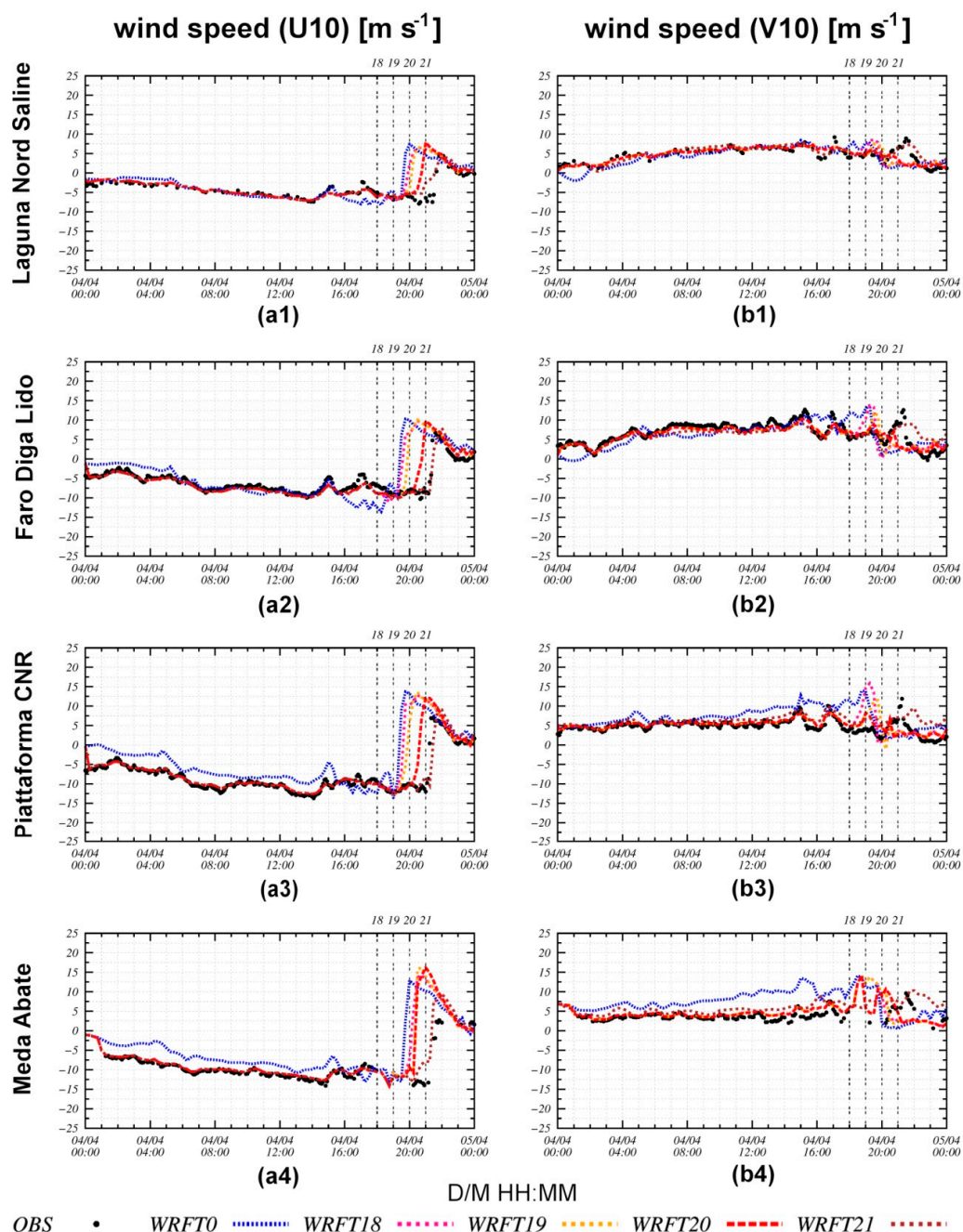


Figure 3. Zonal (left panels) and meridional (right panels) wind components (in $\text{m}\cdot\text{s}^{-1}$) for a selection of weather stations (one for each row), sorted from north to south. Black dots represent the observed values. The blue line shows the values extracted from the inner grid (3 km) of the control run, while the pink, orange and red lines show values extracted from simulations with nudging until 18:00 UTC, 19:00 UTC, and 20:00 UTC, 4 April 2019, respectively.

The reasons for this behavior are provided in Figure 4, which shows the 2 m temperature (colors), the mean sea level pressure (MSLP), and 10 m wind vectors, obtained from the WRF model simulation with observation nudging up to 20:00 UTC (WRFT20). The fields are shown at 14:00 UTC (panel a) and near the occurrence of the high tide, at 20:00 UTC (panel b).

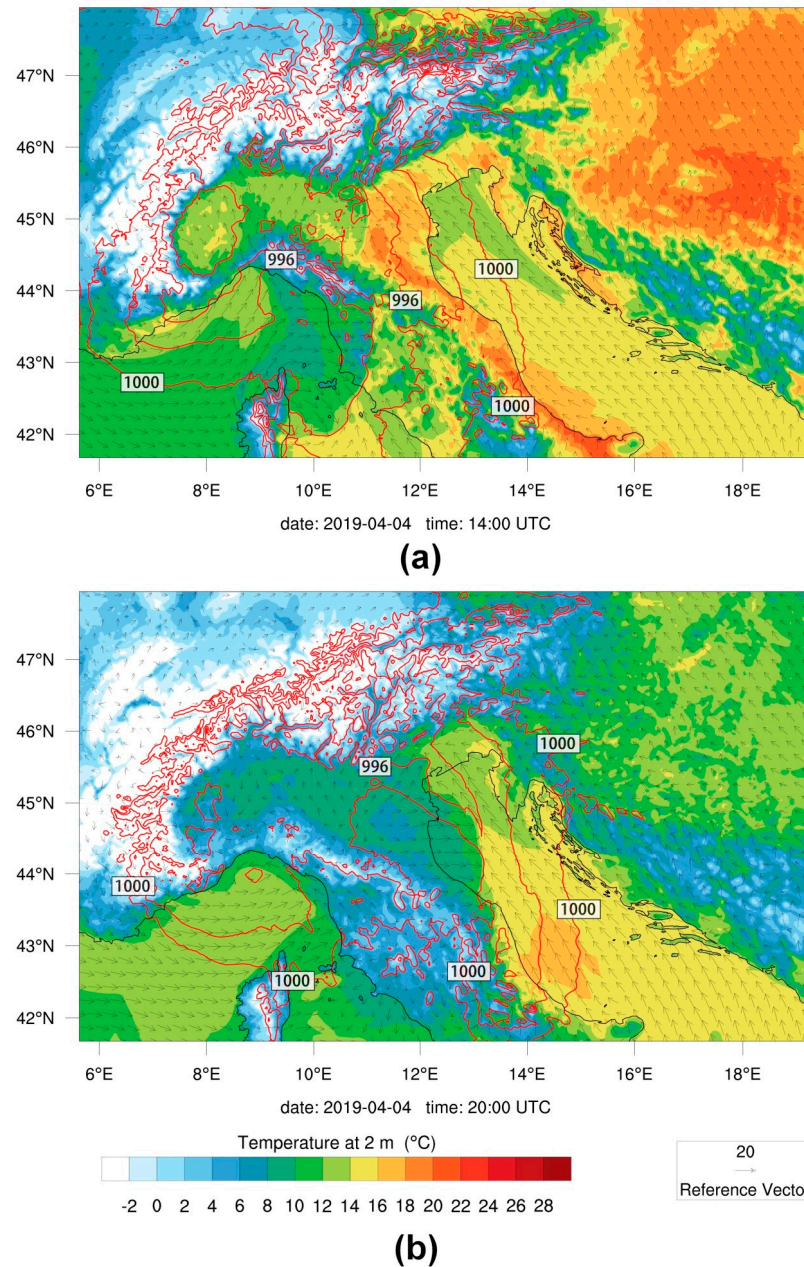


Figure 4. The 2 m temperature (colored scale), mean sea level pressure (red lines, in hPa) and surface wind vectors ($\text{m}\cdot\text{s}^{-1}$) at 14:00 UTC, 4 April 2019 (panel (a)) and at 20:00 UTC, 4 April 2019 (panel (b)). Run with data assimilation until 20:00 UTC, inner grid.

For most of the day, southeasterlies (Sirocco wind) blew over the Adriatic Sea, intensifying from 12:00 UTC onward (Figure 4a). This persistent condition produced a long fetch across the Adriatic from south-east to north-west. From 18:00 UTC onward, a small cold frontal system, moving from west to east, invaded the northern Adriatic (Figure 4b), causing a rapid cooling and wind shifting from the west, that was clearly visible at Piattaforma CNR station around 21:00 UTC (Figure 3). Reasonably, the convergence between the westerlies

behind the frontal system and the southeasterlies ahead of it caused a temporary increase of the sea level height and a delay in the decrease expected from the astronomical tide.

3.2.2. Results and Discussion

For this case study, only the observations of nine surface stations managed by CPSM (identified by red circles in Figure 1b) are available for nudging and for verification. Figure 5 shows the Taylor diagram [22] for 10 m zonal (panel a) and meridional (panel b) wind components in the set of WRF model simulations with nudging ending at 20:00 UTC, 4 April. The simulations are identified in the diagram with different markers. The analysis allows us to evaluate the impact of different model configurations and to select the best tuning of the nudging parameters.

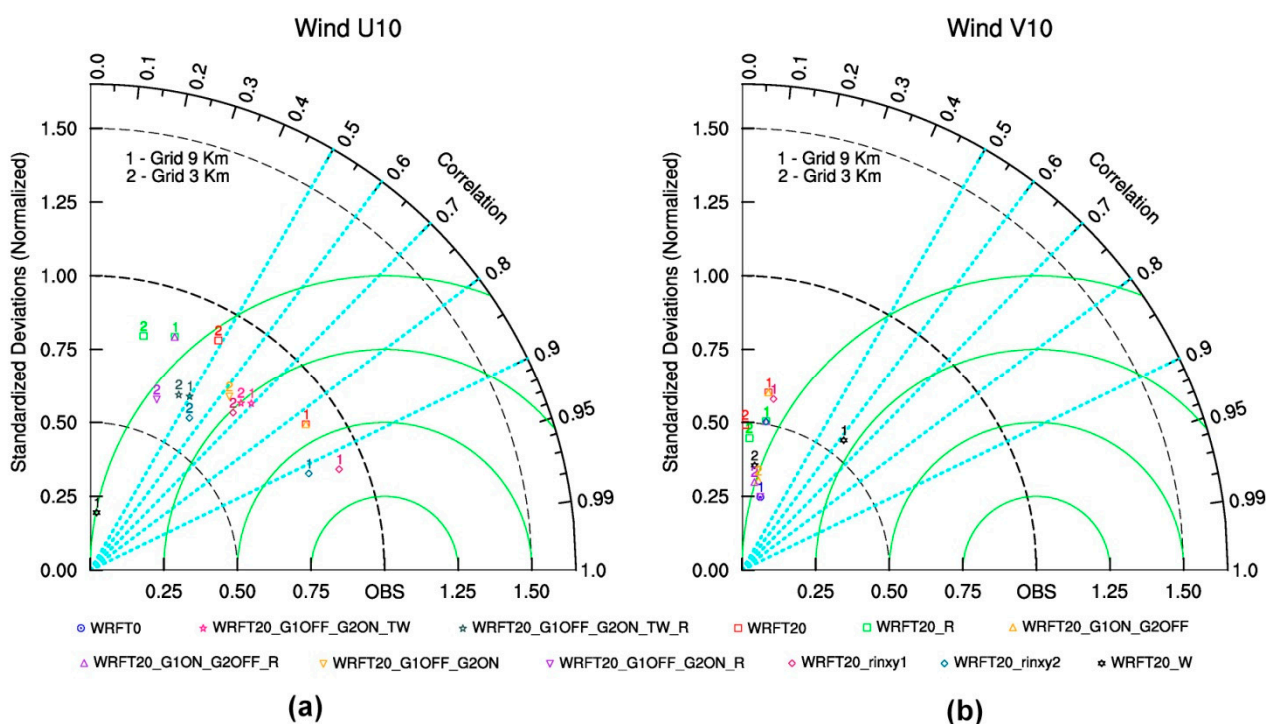


Figure 5. Taylor diagrams, with statistics normalized with respect to observations, for a subset of simulations with data assimilation until 20:00 UTC, except for the control run (blue circles), for the 4 April 2019, case study. (a,b) The zonal and meridional component of the wind, respectively. Numbers 1 and 2 indicate the outer grid (9 km) and the inner grid (3 km), respectively.

The diagrams show three statistical indices:

- (a) The correlation coefficient, related to the azimuthal angle in the diagram (dashed cyan radial lines), measures the pattern similarity between the simulated and observed fields;
- (b) The normalized standard deviation, proportional to the radial distance from the origin (dashed black contours), indicates the relative amplitude of the model and observed variations;
- (c) The centered root-mean-square error in the simulated field is proportional to the distance between each mark and the point on the x-axis identified as “OBS” (green contours). It is a measure of how realistically each simulation (and each grid) reproduces the observations, independently of the model bias.

Statistical indices are calculated considering a subset of the time series, from 20:00 UTC, 4 April, the time the nudging is turned off in this subset of simulations, until 00:00 UTC, 5 April, using data with a temporal frequency of 15 min. Statistics are extracted

comparing the observed wind components with the winds simulated in the grid points that are closest to the weather stations shown in Figure 1b.

In calculating the statistics for the Taylor diagrams, three stations were excluded, namely, Laguna Nord Saline, Meda Abate, and Palazzo Cavalli. The first two suffer from a partial lack of data during the simulation period (respectively 62% and 32% of the data are missing), while wind data are completely missing for the third station.

Each simulation is represented twice in the Taylor diagrams, as results are shown for both the outer and the inner grids, identified with number 1 and 2, respectively. The comparison of the results between the two grids is useful to assess the impact of the horizontal spatial resolution. Considering the small scale of the topographic features and of the meteorological patterns relevant for the two events, the punctual statistical evaluation performed with the Taylor diagram may magnify small errors in time and space, thus having the potential effect of unexpectedly producing worse results for the inner grid, as effectively coming out in the present case study (but not in the second one). This results in worse skill in terms of traditional metrics, such as root-mean-square error (RMSE).

It is difficult to clearly establish which nudging experiment is the best to reproduce the observed evolution, since each configuration performs better for some statistical parameters but not for others. We chose WRFT20 (Table A1, type A) as a reference in the present study considering that, for both wind components (U10 and V10), the model outputs in the inner grid (we are more interested in G2 for future high-resolution operational applications) have the best normalized standard deviation and one of the best correlation coefficients. Run WRFT20_R (Table A1, type B) has a slightly worse performance.

WRFT20_rinxy1 and WRFT20_rinxy2, with reduced horizontal radius of influence, show slightly worse results in terms of correlation and normalized standard deviation for G2, particularly for V10 (the points representing these simulations fall out of the quadrant shown in Figure 5b), while WRFT20_W has correlation values close to zero in the inner grid for both wind components. For WRFT20_G1ON_G2OFF, WRFT20_G1ON_G2OFF_R, WRFT20_G1OFF_G2ON, and WRFT20_G1OFF_G2ON_R, only simulations of type A (i.e., without reduced time window of acquisition) show some skill in terms of correlation and normalized standard deviation, but only in the grid where nudging is active.

The simulation using two-way nesting, with nudging active only in the inner grid, shows correlation and normalized standard deviation comparable to WRFT20, but only for U10. Due to the two-way nesting setup, both grids have very close values of the statistical indices, although G2 is slightly worse than G1.

For the meridional wind component (Figure 5b) all simulations have low correlation values, apart from WRFT20_W in the outer domain. Probably, the weak variation observed for this wind component and the rapid passage of the frontal system makes it more difficult for the model to reproduce the right pattern with the right timing. Conversely, if we consider the zonal wind component, the simulations show a clear improvement due to nudging compared to the control run (which falls out of the quadrant shown here), mainly in the outer grid.

Figure 3 shows the time series of zonal (panel a) and meridional (panel b) wind components, measured in $\text{m}\cdot\text{s}^{-1}$, extracted from the inner grid, for a selection of weather stations (Figure 1b), ordered from north to south. All simulations in this figure have the same model configuration (Table A1, type A). They differ from each other for the different duration of the nudging, which lasts from the beginning of the simulation until 18:00 (WRFT18), 19:00 (WRFT19), 20:00 (WRFT20), and 21:00 UTC (WRFT21), respectively (see Table 2). Observations, the control run (WRFT0), and the whole set of simulations are shown, while the vertical dashed lines represent the time when nudging is turned off in each run.

The left panels of Figure 3 show that, for the zonal wind, the nudging clearly improves the capacity of the model to reproduce the observed wind evolution. In fact, compared to the control run, the nudging allows representing the intensification of the zonal wind

component at a time much closer to the observations, although this does not happen to the same extent for all stations.

In panel a1 (Laguna Nord Saline station), the observed wind component shows a rapid variation from $-7.9 \text{ m}\cdot\text{s}^{-1}$ to $4.8 \text{ m}\cdot\text{s}^{-1}$ between 21:30 and 22:00 UTC. The control run (blue line) can reproduce this pattern but about two hours before, with a similar change in intensity (from $-8.2 \text{ m}\cdot\text{s}^{-1}$ to $7.4 \text{ m}\cdot\text{s}^{-1}$). The longer the nudging is applied, the more the time shift is reduced, achieving the best result for the simulation WRFT21 (brown line), which reproduces a similar change almost at the right time. The intensification of V10 (panel b1) up to $8.9 \text{ m}\cdot\text{s}^{-1}$, around 21:30 UTC, is also well reproduced in WRFT21; all the other simulations with nudging improve the model skill compared to the control run WRFT0, albeit in a more limited way.

Similar considerations apply to the other stations in Figure 3. The improvement in the time evolution of the wind components due to nudging can be better appreciated considering that Laguna Nord Saline and Meda Abate stations (panels (a1,b1) and (a4,b4)) suffer from a partial lack of data.

To analyze how different extensions of the time window for data assimilation may affect the results, Figure 6 shows the Taylor diagrams for the simulations shown in Figure 3, also including the simulations with reduced assimilation time window (type B in Table A1). Only the data after 20:00 UTC, 4 April, are considered for statistical verification.

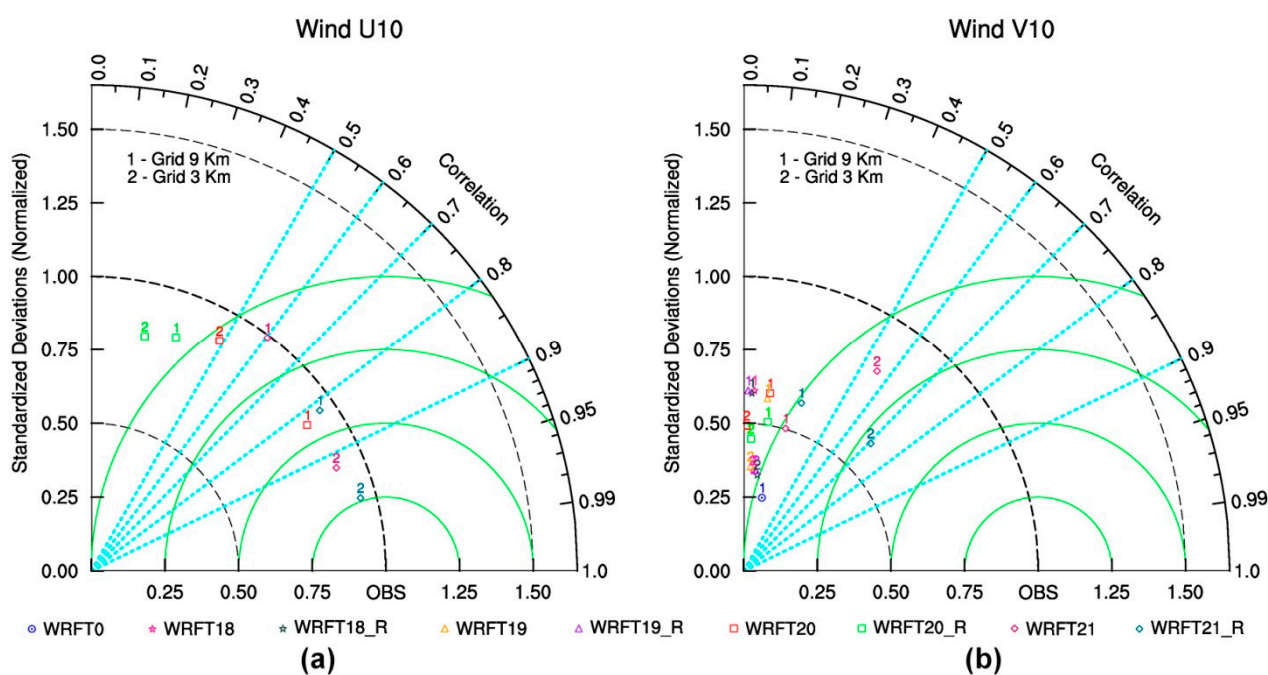


Figure 6. Taylor diagrams for zonal (panel (a)) and meridional (panel (b)) wind components, with statistics normalized with respect to observations. Numbers 1 and 2 indicate the outer grid (9 km) and the inner grid (3 km), respectively. The blue circle identifies the control run while the other marks identify runs with data assimilation until 18:00, 19:00, 20:00, and 21:00 UTC, 4 April 2019.

The best configurations are those for which the nudging ends at 21:00 UTC; their performance is the best in terms of correlation for U10, and in terms of both correlation and normalized standard deviation for V10. The statistical indices in the inner grid are better than in the outer grid, and the simulation with reduced acquisition time window outperforms the other, at least in terms of correlation.

The runs with nudging ending at 20:00 UTC show for U10 similar results as WRFT21 in terms of normalized standard deviation, but slightly worse in terms of correlation. Furthermore, differently from the latter run, the outer grid outperforms the inner grid in

terms of correlation and the run with reduced acquisition window is slightly worse. For V10 the correlation is very weak, although still positive.

The control run and the runs with nudging ending at 18:00 or 19:00 UTC (WRFT0, WRFT18, WRFT18_R, WRFT19, and WRFT19_R) do not appear in the Taylor diagram for U10 because their correlations have negative value for both grids. For V10 (Figure 6b), almost all simulations show very low correlation values and low normalized standard deviation, except for WRFT21 and WRFT21_R, G2 grid.

In conclusion, the nudging leads to improvements in the simulations of this case study, and a wider extension of the acquisition window (WRFT21 and WRFT21_R) leads to better performance. However, the results are not very clear in terms of contribution of the internal grid and of the type B simulations (Table A1).

3.3. Case study 2: 12 November 2019

3.3.1. Description

In this section, the WRF-FDDA data assimilation system is tested for the case study of 12 November 2019 [9]. During this event, a small, but very intense cyclone crossed the northern Adriatic Sea between 19:30 UTC and 21:30 UTC, contributing to an exceptional tide [7] that flooded most of Venice and affected its entire lagoon.

The tide was the result of some concurrent factors: the water pushed northward by the strong Sirocco and deflected westward by the Bora winds, the astronomic tide, the deep small-scale pressure minimum, the very high sea level values observed for several days before the event, and the intense southwesterlies following the passage of the cyclone. The sea level peak in Venice was 189 cm, the second highest since 1872, the year in which data collection began (Figure 7).

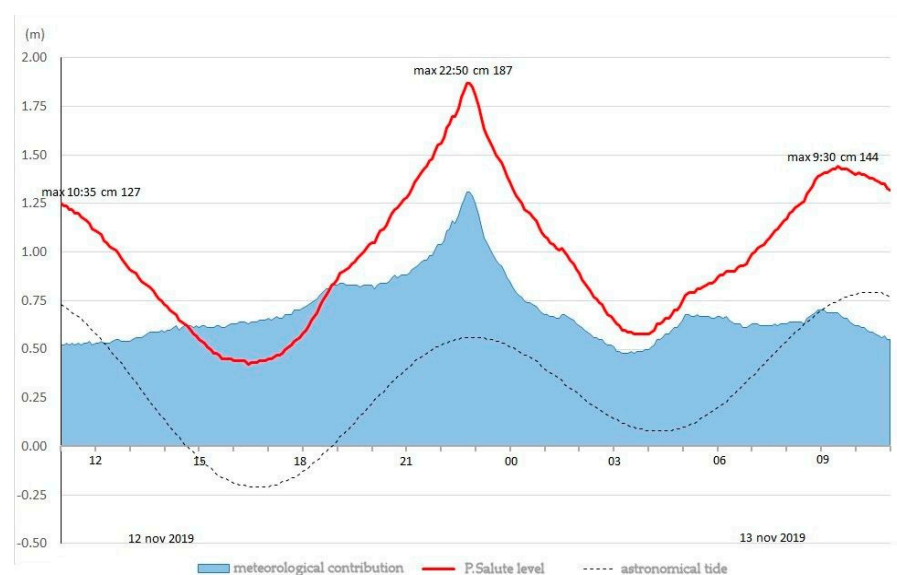
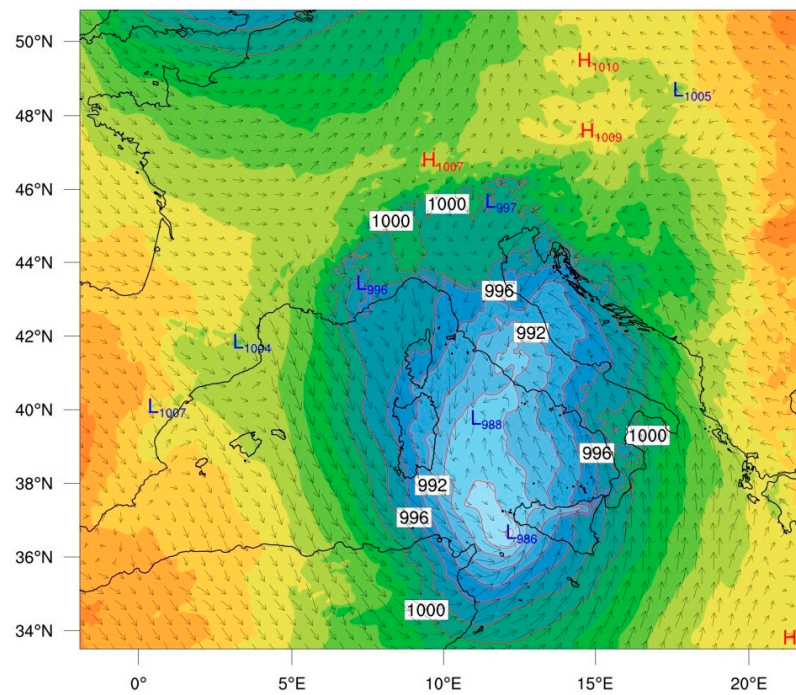


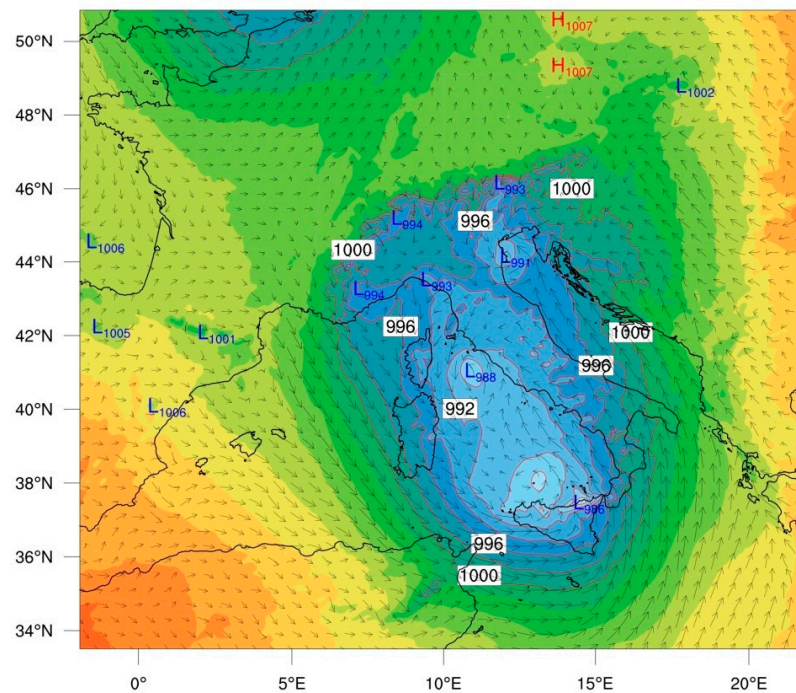
Figure 7. Sea level (red line), storm surge (cyan filled profile), and astronomical tide (dashed line) at “Punta Salute” station, on 12–13 November 2019. The sea level peak in Venice, measured at Punta Salute tide station, on the side of the Giudecca canal, was 189 cm, the second highest since 1872, the year in which data collection began. Time is expressed in UTC+1.

Figure 8 shows the MSLP and 10 m wind fields at 14:00 UTC (panel a) and 20:00 UTC (panel b), obtained from a WRF model simulation with observation nudging up to 22:00 UTC. A small-scale cyclone can be identified on the northern side of a large-scale cyclonic circulation over the Tyrrhenian Sea (Figure 8a), which subsequently moved counterclockwise into the Adriatic Sea. Then, it was pushed by the intense Sirocco wind from the central Adriatic toward the Venice Lagoon, progressively intensifying (Figure 8b) and causing intense wind speeds up to 29 m s^{-1} [9].

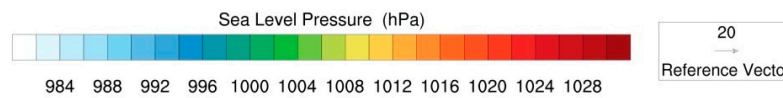


date: 2019-11-12 time: 14:00 UTC

(a)



date: 2019-11-12 time: 20:00 UTC



(b)

Figure 8. Mean sea level pressure (colored scale and red lines, in hPa) and surface wind vectors (m s^{-1}) at 14:00 UTC, 12 November 2019 (panel (a)) and at 20:00 UTC, 12 November 2019 (panel (b)). Run with data assimilation until 22:00 UTC, outer grid.

3.3.2. Results and Discussion

For this case, the observations of 15 stations are available, of which nine were managed by the CPSM and six by ISPRA (identified by red and yellow circles in Figure 1b, respectively). From 12:00 UTC (beginning of the simulation) to 20:00 UTC (just before the end of the nudging periods), Meda Abate station presents a serious lack of data (85% of the total), while wind data in Palazzo Cavalli station are completely missing; thus, these stations provide a poor contribution to the nudging. However, since Meda Abate has complete wind data between 21:00, 12 November and 00:00 UTC, 13 November, i.e., the time window considered for the calculation of the Taylor diagram statistics, it is included in the evaluation of the model performance.

Figure 9 shows the time series of zonal (a) and meridional (b) wind components over a subset of weather stations. Compared to the control run WRFT0, the WRFT22 simulation clearly improves the model skill, reproducing the intensification of the wind due to the passage of the cyclone in terms of amplitude, phase, and shape of the signal, for both wind components. A similar, albeit weaker improvement can also be observed in run WRFT21.

For example, Figure 9a2 shows that, in Malamocco Diga Nord station, the observed zonal wind component (black dots) reaches its maximum ($11.6 \text{ m}\cdot\text{s}^{-1}$) at 22:00 UTC, while the control run (WRFT0; blue line) underestimates the peak ($9.3 \text{ m}\cdot\text{s}^{-1}$) and anticipates its occurrence by about half an hour (at 21:30 UTC). Conversely, in the simulation with nudging ending at 22:00 UTC (WRFT22; red line), the wind reaches its maximum at 22:00 UTC (in phase with the observations), and its peak ($12.1 \text{ m}\cdot\text{s}^{-1}$) is also more realistic.

Furthermore, the time evolution follows the observations much better compared to WRFT0. Although WRFT21 (orange line) underestimates the peak, the wind speed evolution is in phase with the observations. Similar considerations can be applied to V10 (panel b2) and to the other stations in Figure 9.

The Taylor diagrams in Figure 10 give an overall assessment of the nudging performance for this event. Unlike the previous case study, Figure 10 generally shows a better performance for the inner grid compared to the outer domain, in terms of both correlation and normalized standard deviation. The nudging leads to clear improvements in the model skill compared to the control run WRFT0, especially for the inner grid. As shown in Figure 9, the benefit of the assimilation persists for a few hours after the nudging is switched off. A longer period of nudging (WRFT22 and WRFT22_R) is beneficial for the model skill, but some improvements can be observed even in case the nudging ends at 21:00 UTC (WRFT21 and WRFT21_R). Overall, the presence of a reduced time window of data assimilation appears to increase the model skill.

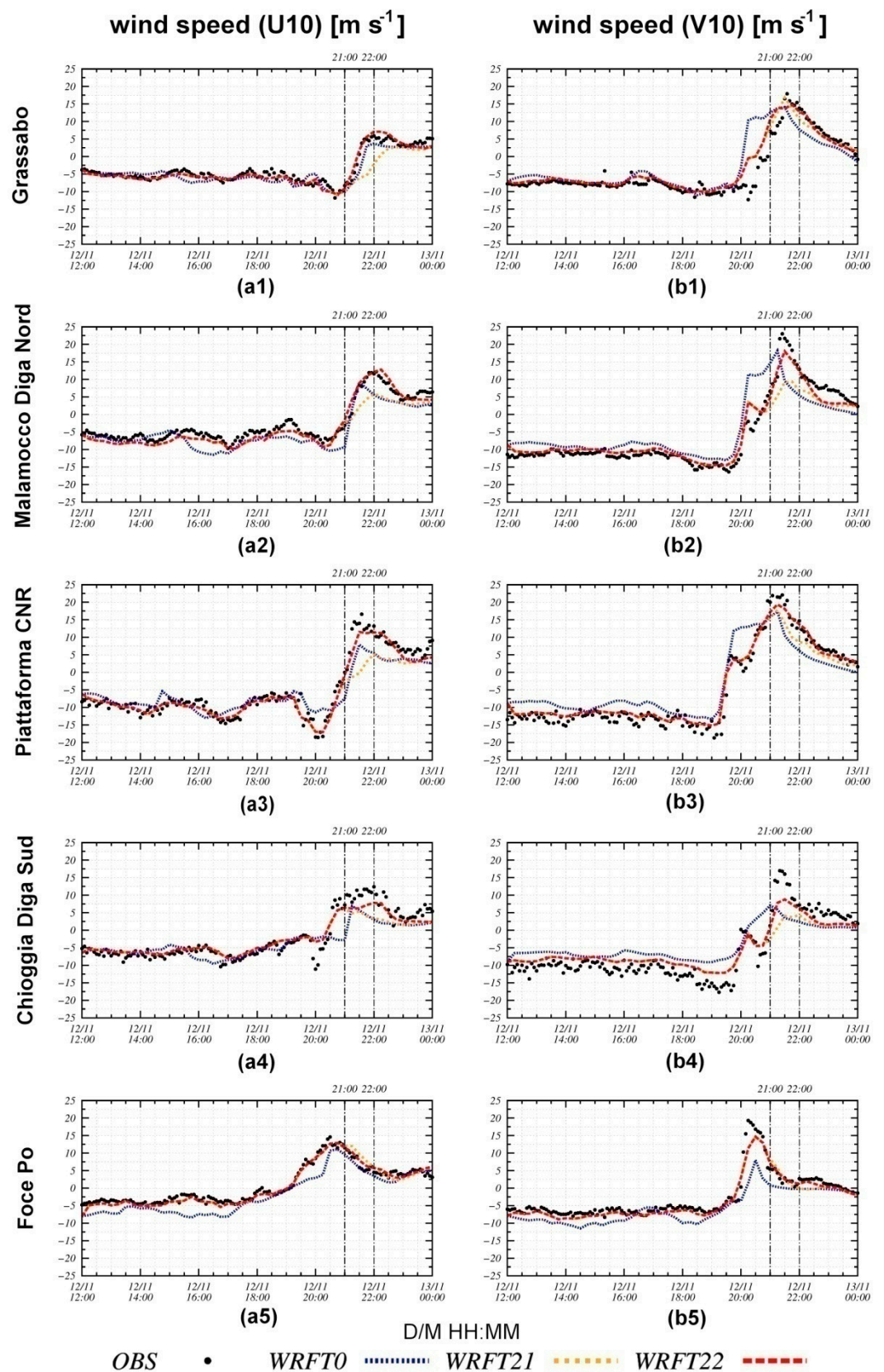


Figure 9. The zonal (left panels) and meridional (right panels) wind components ($m \cdot s^{-1}$) for a selection of weather stations (one for each row), sorted from north to south. Black dots represent the observed values. The blue, orange, and red lines show the values extracted from the inner grid (3 km) of the control run, and the runs with data assimilation until 21:00 UTC and 22:00 UTC on 12 November 2019, respectively.

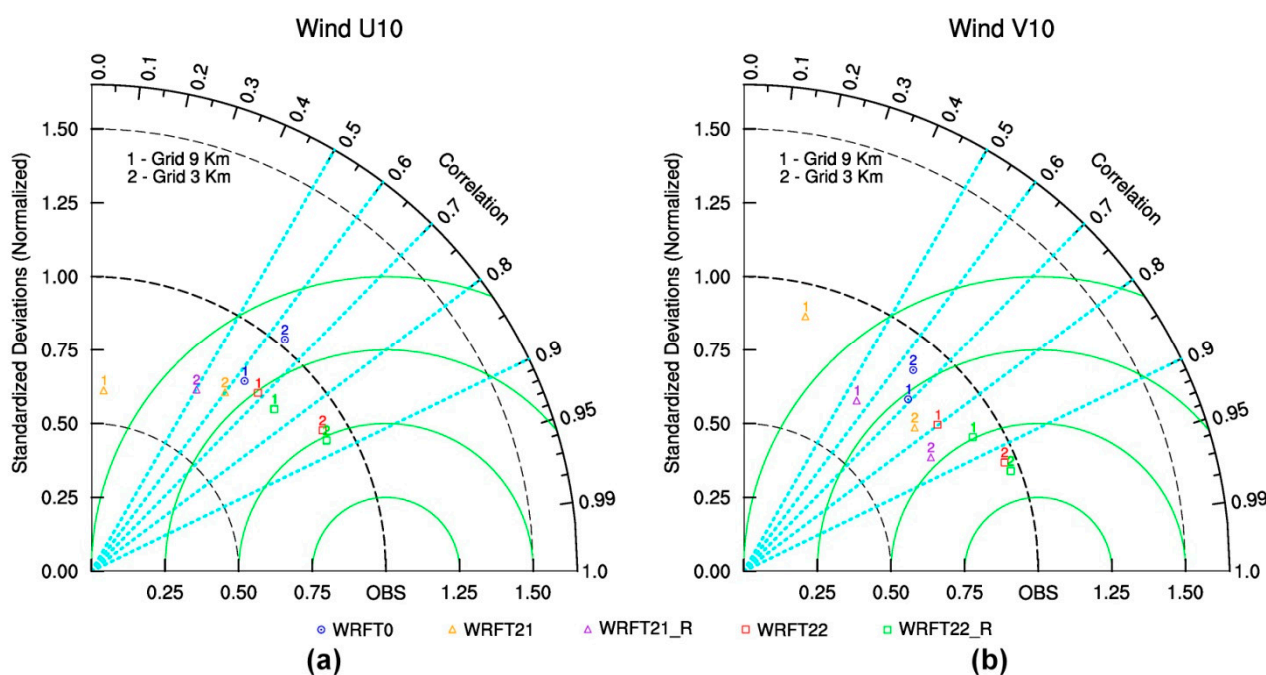


Figure 10. Taylor diagrams for zonal (panel (a)) and meridional (panel (b)) wind components, with statistics normalized with respect to observations. Numbers 1 and 2 indicate the outer grid (9 km) and the inner grid (3 km), respectively. The blue circle identifies the control run. The orange triangle and red square identify runs with data assimilation until 21:00 UTC and 22:00 UTC on 12 November 2019, respectively, while the corresponding runs, with the adjustment of the acquisition time window, are identified by the purple triangle and green square, respectively.

4. Conclusions

The present paper describes the skill of the nudging technique, implemented in the WRF model through the FDDA module, to improve surface wind mesoscale analysis and prediction in an area with complex topography. The numerical system is applied to two high-tide events that occurred in the Venice Lagoon on 4 April 2019 and on 12 November 2019. The motivation for studying these two cases was that the skill of the operational weather forecasts at that time was generally acceptable from a meteorological point of view, but the fine details, which are necessary for impact applications, were completely missed; hence, the real-time prediction of the storm surge was underestimated at its peak by some tens of centimeters. The severity of the tide was misrepresented, with dramatic costs and impact to human activities.

The study is based on the comparison of several numerical simulations in which the model is nudged toward the observed wind fields, measured by a set of meteorological stations distributed inside and in the surrounding areas of the Venice Lagoon. The comparison focused on the final part of the simulations, starting from around the end of the nudging phase, which is in the proximity of the high-tide events, to evaluate the impact of the data assimilation on the model skills.

The results of the 4 April 2019 case study showed that, with the use of data assimilation and higher-resolution grids, the numerical simulations are able to capture better the observation variations in terms of both phase and amplitude, but this improvement appears strongly conditioned by two factors: (1) a long extension of the nudging time period, which should cover the event or at least the phase just before it; (2) the presence of large perturbations in the wind fields (the impact appears relatively minor for the V10 component that is characterized by weaker variations). These aspects lead to further improvement in case a reduced assimilation time window is used (Table A1, type B). In contrast, the absence of these requirements leads to somewhat contradictory results (e.g., the coarse grid

sometimes performs better than the finer one) and, in such conditions, even the tuning of model parameters (such as nesting type and horizontal radius of influence) has a modest and uncertain impact.

The results of the case study of 12 November 2019 show that the nudging provides a clearer improvement for both wind components, especially for the simulation with longer nudging window.

Overall, a positive impact on the forecasting capabilities of the WRF model was due to the use of FDDA, even 2–3 h after the nudging is switched off, in agreement with other applications of the FDDA technique [20,21]. Although the comparison is not completely fair (the period considered for the statistical comparison partially covers the nudging period in the simulations with longer duration of the assimilation window), these results represent an indication of the additional value that this system can provide for nowcasting application aimed at improving wind predictions. A more systematic analysis, covering a longer period, is planned, which should be able to give more conclusive indications also from the perspective of the operational implementation of the numerical system.

The differences in the simulation performance between the two case studies (with overall better results for the case of 12 November 2019) suggest that the FDDA gives a greater improvement in the presence of more intense weather events responsible for stronger variations in the wind components. Further case studies are, however, necessary to generalize these conclusions.

From the perspective of real-time forecasting, the present study shows that the WRF-FDDA represents a useful tool for wind nowcasting even in areas with complex topography. However, an operational application would be computational demanding, as it would require a continuous cycle of assimilation and simulations to be repeated with very high frequency (about 1 h), especially in situations characterized by rapid evolution and strong inhomogeneity.

Author Contributions: D.C., investigation, software, validation, data curation, and writing—original draft preparation; A.T., investigation and writing—original draft preparation; W.C., conceptualization, methodology, and software; A.P., data curation and figure elaboration; M.M.M., supervision, conceptualization, methodology, investigation, and writing—original draft preparation. All authors read and agreed to the published version of the manuscript.

Funding: This work was supported by the Technical–Scientific Collaboration Agreement of CNR-ISAC with the Tide Forecast and Early Warning Center (CPSM)—Civil Protection—Municipality of Venice for the implementation of an experimental data assimilation system for meteorological analysis and forecasting.

Institutional Review Board Statement: Not applicable.

Informed Consent Statement: Not applicable.

Data Availability Statement: The data presented in this study are available on request from the corresponding author.

Acknowledgments: The authors gratefully acknowledge three anonymous reviewers.

Conflicts of Interest: The authors declare no conflict of interest.

Appendix A

The general nudged equation of motion in FDDA has the following form [19]:

$$\frac{\partial Y}{\partial t} = F(Y, t) + G^T W [Y^{obs} - M(Y)], \quad (A1)$$

where Y is the evolving state vector. On the right-hand side of Equation (A1), F represents the background model, Y^{obs} is the vector of observations, and M is the operator that evaluates the model variables at the location of the observations. The difference in squared brackets is the innovation, which is weighted by the product $G^T W$. In turn, G represents the

weighting vector and W is the vector of weighting functions that depends on the temporal and spatial separation between the observations and the model grid variables at time t .

The product $G^T W$ can be set by the user modifying the specific section of the WRF namelist.input file specific for the FDDA. After several trials and errors (partially discussed for the case study of April in Section 3.2.2), two configurations (A and B) were identified and are summarized in Table A1.

Table A1. Relevant parameters used in the FDDA.

	A		B	
	d01 (9 km)	d02 (3 km)	d01 (9 km)	d02 (3 km)
obs_twindo (h)	0.667	0.4	0.667	0.667
obs_rinxy (km)	75	20	75	20
obs_sfcfact	1	1	0.083	0.083
obs_dtramp (min)	0	0	60	60
fdda_end (min)	99,999	99,999	600	600
obs_coef_wind (s^{-1})	7.0×10^{-3}	8.0×10^{-3}	7.0×10^{-3}	8.0×10^{-3}
obs_coef_temp (s^{-1})	7.0×10^{-3}	8.0×10^{-3}	7.0×10^{-3}	8.0×10^{-3}
obs_coef_mois (s^{-1})	7.0×10^{-3}	8.0×10^{-3}	7.0×10^{-3}	8.0×10^{-3}

The first five parameters shown in Table A1 determine the characteristics of the weighting function G in Equation (A1). The parameter obs_twindo and obs_rinxy respectively define the maximum temporal and spatial distance for which an observation is considered in the nudging term. In case of surface observations (as in the present study), obs_twindo is multiplied by the scaling factor obs_sfcfact.

Figure A1 shows the temporal weighting function where, given an observation at time t_0 , the temporal weight linearly increases from 0 at $t_0 - \text{obs_twindo}$ to 1 at $t_0 - \text{obs_twindo}/2$, remains constant until $t_0 + \text{obs_twindo}/2$, and then linearly decreases to 0 at $t_0 + \text{obs_twindo}$ [19].

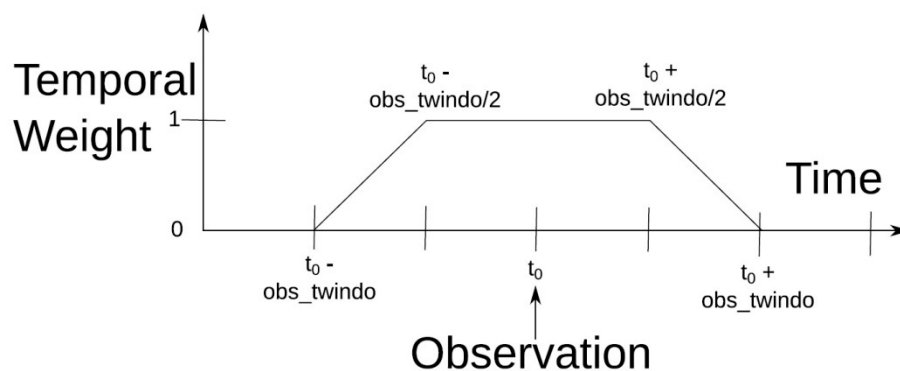


Figure A1. Temporal weighting function for an observation at time t_0 based on the WRF namelist setting obs_twindo.

The parameters obs_dtramp and fdda_end act in combination. In set A, the nudging ends when the last observation is available, and no smoothing is applied apart from the linear decrease in the time window identified with obs_twindo. The configuration B is an example that sets the end of the assimilation after 10 h from beginning of the simulation, but 60 min before the end the nudging term is gradually suppressed by multiplying it for a linear damping factor, which decreases from 1 to 0 in the period.

The last three rows of Table A1 list the weights used for each variable that is assimilated; they correspond to the factor W in Equation (A1).

References

1. Nicholls, R.J.; Wong, P.P.; Burkett, V.R.; Codignotto, J.O.; Hay, J.E.; McLean, R.F.; Ragoonaden, S.; Woodroffe, C.D. Coastal systems and low-lying areas. In *Climate Change 2007: Impacts, Adaptation and Vulnerability. Contribution of Working Group II to the Fourth Assessment Report of the Intergovernmental Panel on Climate Change*; Parry, M.L., Canziani, O.F., Palutikof, J.P., van der Linden, P.J., Hanson, C.E., Eds.; Cambridge University Press: Cambridge, UK, 2007; pp. 315–356.
2. Woodworth, P.L.; Melet, A.; Marcos, M.; Ray, R.D.; Wöppelmann, G.; Sasaki, Y.N.; Cirano, M.; Hibbert, A.; Huthnance, J.M.; Monserrat, S.; et al. Forcing Factors Affecting Sea Level Changes at the Coast. *Surv. Geophys.* **2019**, *40*, 1351–1397. [[CrossRef](#)]
3. Vilibić, I.; Šepić, J.; Pasarić, M.; Orlić, M. The Adriatic Sea: A long-standing laboratory for sea level studies. *Pure Appl. Geophys.* **2017**, *174*, 3765–3811. [[CrossRef](#)]
4. Vilibić, I.; Denamiel, C.; Zemunik, P.; Monserrat, S. The Mediterranean and Black Sea meteotsunamis: An overview. *Nat. Hazards* **2020**, *106*, 1223–1267. [[CrossRef](#)]
5. Lionello, P.; Nicholls, R.J.; Umgiesser, G.; Zanchettin, D. Venice flooding and sea level: Past evolution, present issues, and future projections (introduction to the special issue). *Nat. Hazards Earth Syst. Sci.* **2021**, *21*, 2633–2641. [[CrossRef](#)]
6. Umgiesser, G. The impact of operating the mobile barriers in Venice (MOSE) under climate change. *J. Nat. Conserv.* **2020**, *54*, 125783. [[CrossRef](#)]
7. Ferrarin, C.; Bajo, M.; Benetazzo, A.; Cavaleri, L.; Chiggiato, J.; Davison, S.; Davolio, S.; Lionello, P.; Orlić, M.; Umgiesser, G. Local and large-scale controls of the exceptional Venice floods of November 2019. *Prog. Oceanogr.* **2021**, *197*, 102628. [[CrossRef](#)]
8. Ferrarin, C.; Lionello, P.; Orlić, M.; Raicich, F.; Salvadori, G. Venice as a paradigm of coastal flooding under multiple compound drivers. *Sci. Rep.* **2022**, *12*, 5754. [[CrossRef](#)] [[PubMed](#)]
9. Miglietta, M.M.; Buscemi, F.; Dafis, S.; Papa, A.; Tiesi, A.; Conte, D.; Davolio, S.; Flaounas, E.; Levizzani, V.; Rotunno, R. A high-impact meso-beta vortex in the Adriatic Sea. *QJRMS* **2023**. [[CrossRef](#)]
10. Skamarock, W.C.; Klemp, J.B.; Dudhia, J.; Gill, D.O.; Liu, Z.; Berner, J.; Wang, W.; Powers, J.G.; Duda, M.G.; Barker, D.M.; et al. *A Description of the Advanced Research WRF Model Version 4*; No. NCAR/TN-556+STR; National Center for Atmospheric Research: Boulder, CO, USA, 2019.
11. Thompson, G.; Field, P.R.; Rasmussen, R.M.; Hall, W.D. Explicit forecasts of winter precipitation using an improved bulk microphysics scheme. Part II: Implementation of a new snow parameterization. *Mon. Weather Rev.* **2008**, *136*, 5095–5115. [[CrossRef](#)]
12. Mlawer, E.J.; Taubman, S.J.; Brown, P.D.; Iacono, M.J.; Clough, S.A. Radiative transfer for inhomogeneous atmospheres: RRTM, a validated correlated-k model for the longwave. *J. Geophys. Res.* **1997**, *102*, 16663–16682. [[CrossRef](#)]
13. Dudhia, J. Numerical study of convection observed during the Winter Monsoon experiment using a mesoscale two-dimensional model. *J. Atmos. Sci.* **1989**, *46*, 3077–3107. [[CrossRef](#)]
14. Jiménez, P.A.; Dudhia, J.; González-Rouco, J.F.; Navarro, J.; Montávez, J.P.; García-Bustamante, E. A revised scheme for the wrf surface layer formulation. *Mon. Weather Rev.* **2012**, *140*, 898–918. [[CrossRef](#)]
15. Fairall, C.W.; Bradley, E.F.; Hare, J.E.; Grachev, A.A.; Edson, J.B. Bulk parameterization of air-sea fluxes: Updates and verification for the COARE algorithm. *J. Clim.* **2003**, *16*, 571–591. [[CrossRef](#)]
16. Tewari, M.; Chen, F.; Wang, W.; Dudhia, J.; LeMone, M.A.; Mitchell, K.; Ek, M.; Gayno, G.; Wegiel, J.; Cuenca, R.H. Implementation and verification of the unified NOAA land surface model in the WRF model. In Proceedings of the 20th Conference on Weather Analysis and Forecasting/16th Conference on Numerical Weather Prediction, Seattle, WA, USA, 12–16 January 2004; American Meteorological Society: Boston, MA, USA, 2004.
17. Hong, S.-Y.; Lim, J.-O.J. The WRF single-moment 6-class microphysics scheme (WSM6). *J. Korean Meteorol. Soc.* **2006**, *42*, 129–151.
18. Kain, J.S. The Kain–Fritsch convective parameterization: An update. *J. Appl. Meteorol.* **2004**, *43*, 170–181. [[CrossRef](#)]
19. Reen, B. A Brief Guide to Observation Nudging in WRF, Battlefield Environment Division, Army Research Laboratory February 2016. Available online: <https://www2.mmm.ucar.edu/wrf/users/docs/ObsNudgingGuide.pdf> (accessed on 1 February 2020).
20. Chen, D.S.; Hsiao, L.F.; Xie, J.H.; Peng, M.S.; Fong, C.T.; Chang, P.L.; Fang, W.T.; Hong, J.S.; Yeh, T.C. Impacts of assimilating dual-doppler radar-retrieval winds on the twrf predictions of typhoon Nesat (2017). *Terr. Atmos. Ocean. Sci.* **2021**, *32*, 649–667. [[CrossRef](#)]
21. Sun, H.; Wang, H.; Yang, J.; Zeng, Y.; Zhang, Q.; Liu, Y.; Gu, J.; Huang, S. Improving Forecast of Severe Oceanic Mesoscale Convective Systems Using FY-4A Lightning Data Assimilation with WRF-FDDA. *Remote Sens.* **2022**, *14*, 1965. [[CrossRef](#)]
22. Taylor, K.E. Summarizing multiple aspects of model performance in a single diagram. *Atmospheres* **2001**, *106*, 7183–7192. [[CrossRef](#)]

Disclaimer/Publisher’s Note: The statements, opinions and data contained in all publications are solely those of the individual author(s) and contributor(s) and not of MDPI and/or the editor(s). MDPI and/or the editor(s) disclaim responsibility for any injury to people or property resulting from any ideas, methods, instructions or products referred to in the content.